Contrasting responses of vegetation productivity to intraseasonal rainfall in Earth system models

Earth Syst. Dynam., 15, 1019–1035, 2024
https://doi.org/10.5194/esd-15-1019-2024

Earth System Dynamics
Open Access
EGU

Contrasting responses of vegetation productivity to intraseasonal rainfall in Earth system models

Bethan L. Harris[1], **Tristan Quaife**[2], **Christopher M. Taylor**[1], **and Phil P. Harris**[1]

[1]National Centre for Earth Observation, UK Centre for Ecology & Hydrology, Wallingford, UK
[2]National Centre for Earth Observation, Department of Meteorology, University of Reading, Reading, UK

Correspondence: Bethan L. Harris (bethar@ceh.ac.uk)

Received: 8 January 2024 – Discussion started: 19 January 2024
Revised: 23 May 2024 – Accepted: 18 June 2024 – Published: 6 August 2024

Abstract. Correctly representing the response of vegetation productivity to water availability in Earth system models (ESMs) is essential for accurately modelling the terrestrial carbon cycle and the evolution of the climate system. Previous studies evaluating gross primary productivity (GPP) in ESMs have focused on annual mean GPP and interannual variability, but physical processes at shorter timescales are important for determining vegetation–climate coupling. We evaluate GPP responses at the intraseasonal timescale in five CMIP6 ESMs by analysing changes in GPP after intraseasonal rainfall events with a timescale of approximately 25 d. We compare these responses to those found in a range of observation-based products. When composited around all intraseasonal rainfall events globally, both the amplitude and the timing of the GPP response show large inter-model differences, demonstrating discrepancies between models in their representation of water–carbon coupling processes. However, the responses calculated from the observational datasets also vary considerably, making it challenging to assess the realism of the modelled GPP responses. The models correctly capture the fact that larger increases in GPP at the regional scale are associated with larger increases in surface soil moisture and larger decreases in atmospheric vapour pressure deficit. However, the sensitivity of the GPP response to these drivers varies between models. The GPP in NorESM is insufficiently sensitive to vapour pressure deficit perturbations when compared all to other models and six out of seven observational GPP products tested. Most models produce a faster GPP response where the surface soil moisture perturbation is larger, but the observational evidence for this relationship is weak. This work demonstrates the need for a better understanding of the uncertainties in the representation of water–vegetation relationships in ESMs and highlights a requirement for future daily-resolution observations of GPP to provide a tighter constraint on global water–carbon coupling processes.

1 Introduction

The flux of carbon into the land surface resulting from photosynthesis is referred to as gross primary productivity (GPP). Terrestrial GPP is the single largest component flux in the global carbon cycle, with typical estimates of its magnitude being in the region of 140 $\mathrm{Pg\,C\,a^{-1}}$ (Canadell et al., 2021). As such, it plays a key role in modulating the atmospheric carbon dioxide concentration, and the terrestrial biosphere has taken up around a third of anthropogenic CO_2 emissions over recent decades (Friedlingstein et al., 2022). Understanding the processes that control this uptake is critical to our ability to correctly model climate because any change has potentially significant implications for the accumulation of CO_2 in the atmosphere. Relevant processes include a number of limiting factors, such as the availability of nutrients (Fernández-Martínez et al., 2014), fertilisation by atmospheric carbon dioxide (Chen et al., 2022), and water – the focus of this study – in terms of both soil moisture that is accessible to plants and the atmospheric vapour pressure deficit.

Without sufficient available water for transpiration, or when there is high atmospheric demand (corresponding to a high vapour pressure deficit, VPD), plants close their stom-

ata. As a consequence, they are unable to replenish leaf-internal carbon dioxide, and thus photosynthesis is downregulated. The water and carbon cycles are thus intrinsically linked, and the availability of water is a first-order determinant of terrestrial GPP. There is growing evidence that the growth rate of atmospheric CO_2 is sensitive to changes in terrestrial water storage (Humphrey et al., 2018; Liu et al., 2023) and a reasonable hypothesis is that this signal is in part controlled by the response of photosynthesis to water availability in soil. In climate models, the representation of downregulation of GPP due to lack of available soil water is typically quite crude. A commonly used approach is to model the potential, un-stressed GPP and then apply a scalar which is determined by a linear ramp between some bounds, below which no photosynthesis occurs and above which it is unaffected by soil moisture. This avoids the complexities of implementing more process-based schemes, such as that of Bonan et al. (2014), into climate models, as these introduce additional poorly constrained parameterisations. However, the schemes currently employed are sensitive to choices such as soil hydraulic parameters and the depth over which the soil moisture stress factor is calculated (Harper et al., 2021). These decisions, implemented by modelling groups, will lead to differences in the response of the modelled GPP to soil moisture.

It is generally the case that the stomatal conductance decreases with increasing VPD and hence lowers the rate at which CO_2 is drawn into the substomatal cavity to replenish that used in photosynthesis. However, empirical studies reveal a complex relationship between water use efficiency (WUE, the amount of carbon assimilation per unit of water transpired) and VPD, and consequently, the relationship with GPP is not straightforward (Grossiord et al., 2020). The land surface components of many climate models use variants of the Ball–Berry scheme (Ball et al., 1987). This approach relates the stomatal conductance to the carbon assimilation and atmospheric humidity via empirical parameters, assuming a linear response. Commonly used extensions to Ball–Berry in climate models, in particular that developed by Leuning (1995), provide more realistic responses of stomatal conductance to VPD but still rely on empirical parameterisation and do not appear to have much additional skill over the original Ball–Berry model when used for large-scale simulations (Knauer et al., 2015). As a consequence the relationship between GPP and VPD in climate models remains fairly crude. A key assumption in many climate models is that the slope of the relationship between stomatal conductance and VPD can be assigned globally (often on the basis of plant functional type) and is not affected by environmental conditions (Knauer et al., 2015). A further confounding factor is that the interpretation of the effects of VPD and soil moisture on GPP tend to be complicated by their interdependence on each other. High VPD will generally coincide with dry soils and vice versa due to feedbacks between surface energy and water fluxes and the lower atmosphere.

A key problem in trying to evaluate the processes in climate models involved in the water controls on photosynthesis in models is that observations of GPP on large spatial scales tend to be heavily modelled themselves. For example, the MODIS GPP product (MOD17) is based on a light use efficiency approach where the primary satellite data input is the fraction of absorbed photosynthetically active radiation (Running et al., 2004). The efficiency by which the absorbed light is used to drive carbon assimilation is modelled, with meteorological drivers as inputs. Consequently, any difference between GPP predicted by a climate model and the corresponding MODIS data could be due to the modelled efficiency term in MOD17. Arguably, a better point of contact between the models and the MODIS data would be the fraction of absorbed photosynthetically active radiation (fAPAR) itself as this is more directly derived from the actual satellite observations (Zobitz et al., 2014), but this contains no direct information about water.

Another approach to estimating GPP on global scales, which has been gaining much traction in recent years, is to upscale eddy-covariance-based estimates of GPP from flux tower networks using Earth observation (EO) and meteorological data as inputs to regression models. The FLUXCOM GPP product, for example, uses a wide range of data from the MODIS sensors, including vegetation indices and land cover data, meteorological data from ERA-Interim, and a range of machine learning techniques to upscale the FLUXNET data record (Jung et al., 2020; Tramontana et al., 2016). Whilst these methods show great promise, their reliance on the flux towers means that the data they are trained on contain sampling bias toward northern temperate regions, with relatively few data across the tropics. This is particularly problematic as the majority of global GPP occurs in these tropical regions, so this data scarcity is a key contributor to uncertainty in global total GPP (Schimel et al., 2015). The tropics are also likely to be a key region in which water will influence vegetation productivity as the climate changes (Worden et al., 2021).

Solar-induced fluorescence (SIF) observations from space offer a new and potentially transformative information source on large-scale GPP (Pickering et al., 2022). SIF is a by-product of photosynthesis, and observations are hence directly related to the biochemical mechanisms controlling GPP in a way not available from other global-scale data sources. However, mechanistic estimates of GPP from satellite-observed SIF are not yet routinely available, and most existing products are generated using statistical regression (Bai et al., 2022; Alemohammad et al., 2017). In addition, the EO-based SIF data record is relatively short, with longer-term data records (such as from GOSAT) having relatively sparse spatial sampling.

Previous evaluations of GPP in global models have typically focused on annual mean GPP, interannual variability, and trends (Piao et al., 2013; Anav et al., 2015; Slevin et al., 2017; Kim et al., 2018; Hu et al., 2022). These studies have

shown that although models can produce reasonable spatial and seasonal distributions of GPP, there is a large inter-model range in mean global GPP (Piao et al., 2013; Anav et al., 2015; Kim et al., 2018; Hu et al., 2022). The observation-based products used for evaluation also have large differences in mean global GPP (Anav et al., 2015). Models produce a mean annual GPP that is sensitive to interannual variations in temperature, precipitation, and radiation (Piao et al., 2013; Anav et al., 2015), but there is uncertainty in the magnitude of the GPP interannual variability, and it tends to be too weak in observation-based products compared to models.

However, studies using daily observational data have shown that vegetation also responds to intraseasonal variability in precipitation (Guan et al., 2014; Wu et al., 2022; Harris et al., 2022). Evaluating modelled GPP responses at these shorter timescales offers an opportunity to investigate the physical processes linking climate drivers to GPP. In many regions, the intraseasonal variability of vegetation strongly influences vegetation–climate coupling out to interannual timescales (Guan et al., 2014, 2018; Wu et al., 2021; Barnes et al., 2021). Correctly modelling GPP responses to shorter-term variations in precipitation could therefore improve estimates of land carbon uptake on climate-relevant timescales.

Here, we investigate how GPP (and other linked variables, such as soil moisture and vapour pressure deficit) responds to intraseasonal precipitation events in different CMIP6 models and assess against a range of observation-based GPP products to get physical insight into which models have realistic rainfall–GPP coupling processes. An issue in comparing climate model outputs in terms of their rainfall–GPP responses is that the timing, magnitude, and location of precipitation events are likely to be inconsistent. Consequently any differences in the modelled GPP could be due to differences in the simulation of the rainfall regime itself. The approach we have adopted is to identify the timing of peak intraseasonal precipitation events (Harris et al., 2022) and compare the response of other variables relative to that point in time. We show that, whilst models agree on the timescales of the response of soil moisture to precipitation events, there are considerable discrepancies between models in the response of GPP to precipitation. This points to disagreement in the processes that couple available water and GPP in the models. Furthermore, we note that observational GPP products also exhibit similar levels of disagreement in the timing of response of GPP to rainfall, pointing to the need for better data products.

2 Data and methods

2.1 CMIP6 model data

We compare vegetation productivity responses in models from the CMIP6 *esm-hist* experiment (Eyring et al., 2016). This experiment covers the recent historical period from 1850 to 2014. Only data from 2000–2014 are included in our analysis in order to permit a fair comparison with the available satellite observations. To investigate vegetation productivity responses to intraseasonal rainfall variability, we require daily or sub-daily model output data for precipitation and GPP. These data are available for the *esm-hist* experiment for only five models: ACCESS-ESM1-5, BCC-CSM2-MR, CNRM-ESM2-1, NorESM2-LM, and UKESM1-0-LL. We use the precipitation fields provided at daily resolution and take the daily mean of the GPP data, which is made available at 3 h resolution. These models also all provide daily surface soil moisture (mrsos) data: this is the mass of water in the upper 10 cm of soil. We compute daily near-surface VPD from near-surface air temperature (tas) and relative humidity (hurs). This is done by first computing the saturation vapour pressure e_s according to Tetens' formula (Bolton, 1980):

$$e_s = 6.112 \exp\left(\frac{17.67 \times \text{tas}}{\text{tas} + 243.5}\right), \quad (1)$$

where tas is expressed in degrees Celsius (°C). The vapour pressure deficit is then

$$\text{VPD} = e_s\left(1 - \frac{\text{hurs}}{100}\right). \quad (2)$$

Near-surface relative humidity is not available at daily resolution for BCC-CSM2-MR, so this model is excluded from the VPD-focused sections of our analysis. All model data are regridded to $1° \times 1°$ horizontal resolution using land-area-weighted averaging.

2.2 Observational datasets

Intraseasonal rainfall events are identified using the Integrated Multi-satellitE Retrievals for GPM (IMERG) V06 daily product (Huffman et al., 2019). Surface soil moisture is assessed using both the ESA CCI Soil Moisture combined active–passive microwave product v06.1 (Dorigo et al., 2017; Gruber et al., 2019) and the Global Land Evaporation Amsterdam Model (GLEAM) v3.6a (Miralles et al., 2011; Martens et al., 2017). GLEAM models the distribution of soil water content based on Multi-Source Weighted-Ensemble Precipitation (MSWEP) v2.8 (Beck et al., 2017) and corrects the soil moisture of the top model layer by assimilating the ESA CCI Soil Moisture combined product. The two surface soil moisture datasets are therefore not independent, but both are tested here to ascertain whether the differences in the products affect the assessment of the CMIP6 models' surface soil moisture. ESA CCI Soil Moisture has the advantage of being less reliant on model algorithms, while the surface soil layer in GLEAM is 10 cm deep and may therefore be more representative of the CMIP mrsos variable, which is defined over the same depth. The microwave observations used in ESA CCI Soil Moisture measure varying soil depths but are typically taken to quantify soil moisture in the top 2–5 cm (Ulaby et al., 1982). We compute near-surface VPD

from ERA5 reanalysis data for 2 m air temperature and 2 m dew-point temperature (Hersbach et al., 2020).

Daily GPP data are obtained from FLUXCOM RS+METEO (Jung et al., 2020). FLUXCOM RS+METEO uses machine learning to upscale estimates of terrestrial carbon fluxes from eddy covariance flux towers to create a global gridded GPP product based on remote sensing and meteorological forcing data. We test versions of FLUXCOM RS+METEO using two different meteorological forcing datasets: ERA5 and CRU JRA v1.1 (Harris et al., 2014; Kobayashi et al., 2015; Harris, 2019). For each of these forcing datasets, we use the ensemble median GPP over three machine learning methods and two flux partitioning methods, as detailed by Tramontana et al. (2016) and Jung et al. (2019). Note that while the meteorological forcing data are updated daily, the remote sensing driving data are based on mean seasonal cycles (Jung et al., 2020).

Whilst daily data are preferable for investigating intraseasonal variability, information can also be obtained from other sub-monthly GPP datasets. Incorporating these datasets into the analysis allows a better understanding of the uncertainty in our results that arises from the need to derive GPP from direct observations. We include the 8-daily MODIS Terra GPP product (Running et al., 2015), as quality-controlled and regridded by Kern (2021). We also analyse the 8-daily VPM GPP product (Zhang et al., 2017a), which is intended to provide an alternative to MODIS Terra GPP by using the improved light use efficiency theory of the vegetation photosynthesis model (VPM). The VODCA2GPP dataset (Wild et al., 2022), which estimates GPP based on vegetation optical depth (VOD) retrieved from passive microwave observations, is also produced at 8 d resolution.

Satellite observations of solar-induced chlorophyll fluorescence (SIF) provide an additional way of estimating GPP at the global scale. SIF is approximately linearly correlated with GPP (Frankenberg et al., 2011), although the relationship varies with season and vegetation type (Chen et al., 2021). We therefore also compare the modelled GPP responses with SIF data that are spatially downscaled from GOME-2 observations (Duveiller et al., 2020). This product includes data based on two different methods of retrieval from GOME-2: Joiner et al. (2013), henceforth labelled JJ, and Köhler et al. (2015), labelled PK. These datasets have a temporal resolution of 8 d using a 16 d rolling window.

All observational products are available for the complete period 2000–2014, except for IMERG, which is available from June 2000 onwards, and the GOME-2 SIF data, which are available from 2007 onwards. All products are regridded by land-area-weighted averaging to a horizontal resolution of $1° \times 1°$.

2.3 Compositing around intraseasonal precipitation events

Intraseasonal precipitation events are identified using the method of Harris et al. (2022). Long-term linear temporal trends in the data are removed before processing. For each $1° \times 1°$ grid box, we apply a 25 d low-pass Lanczos filter to the daily precipitation anomaly, where the anomaly is computed relative to the climatology for a 7 d rolling window. This removes variability at frequencies higher than 25 d from the anomaly time series. Intraseasonal precipitation events are then defined as local maxima of the filtered time series that lie above 1 standard deviation from the mean. This method identifies wetter-than-usual intraseasonal periods with a characteristic timescale of approximately 25 d. The elevated precipitation associated with an intraseasonal wet event may be a single large rainfall event or it may comprise several shorter bursts of rainfall. Using such a filtering approach ensures that the driving precipitation composites have a consistent timescale so that they provide a fair basis on which to compare the timescales of the GPP responses between the models and the observations. The dates of these events are identified separately for each CMIP6 model and for IMERG. Due to gaps in the IMERG dataset at high latitudes, this procedure results in far fewer observed events than modelled events outside the latitude band 60° S–60° N. We therefore restrict all analyses of both modelled and observational data to 60° S–60° N in order to ensure a fair comparison between the two. We then composite daily standardised anomalies (relative to 7 d rolling climatology) of precipitation, SSM, VPD, and GPP around the dates of the intraseasonal precipitation events. For the observational GPP products with 8 d resolution, the standardised anomalies are computed relative to a 31 d rolling climatology instead of 7 d to ensure sufficient data for the climatological averaging. It should be noted that the composited variables do not undergo Lanczos filtering; the filter is only used to determine the dates of the precipitation events around which to composite.

The results are aggregated over regions containing multiple grid boxes to increase the number of precipitation events contributing to each composite. Only grid boxes with valid ESA CCI Soil Moisture observations are included to maximise our observational knowledge of the surface soil moisture perturbations that are driving the GPP responses. Although this eliminates tropical forest regions from the analysis, it is found to make only a small difference to the resulting GPP composites, since vegetation in these regions does not respond strongly to intraseasonal wet events compared to vegetation in water-limited regions (Harris et al., 2022). We also remove frozen grid boxes from the composites by discarding events in months when the median of maximum 2 m air temperature is below 0 °C.

3 Results

3.1 Global evaluation

Global (60° S–60° N) composites of precipitation, surface soil moisture, and GPP around intraseasonal wet events are shown in Fig. 1. The composites of precipitation are similar between the CMIP6 models and observations (Fig. 1a), indicating that our method successfully creates similar standardised anomalies of precipitation driving the land surface responses in each case. The surface soil moisture responses following these wet events are also similar between models (Fig. 1b), with consistent maximum standardised anomalies 2–3 d after the wet event peak and comparable longer-term anomalies of elevated soil moisture out to 60 d. The observed surface soil moisture composites from the GLEAM and ESA CCI products are also a reasonable match to the CMIP6 models. The models are in better agreement with the observed composite obtained from GLEAM, which may be due to GLEAM representing the same depth of soil surface layer as the model output.

However, the responses of GPP to the intraseasonal wet events show large inter-model differences (Fig. 1c). All models exhibit a positive GPP anomaly in the days following the peak of wet events, but the amplitude and timing of this anomaly vary greatly. CNRM-ESM and UKESM produce a larger standardised anomaly in GPP than the other models, while ACCESS-ESM and NorESM show the smallest responses. NorESM also has the slowest response in GPP, with the peak GPP anomaly occurring 22 d after the peak precipitation anomaly compared to 4 d for BCC-CSM, the fastest-responding model. The models also show contrasting behaviour leading up to the peak of the wet events: some have a much larger negative GPP anomaly than others, associated with a reduction in downwelling shortwave radiation during the wet events. However, in this study we focus on the post-event characteristics of the GPP response.

To investigate which of the modelled productivity responses are realistic, the wet event GPP composites are shown in Fig. 1d for a variety of datasets based on observations (as described in Sect. 2). While composites obtained from the same family of observational products (e.g. the two SIF retrieval methods) are similar to one another, there is a large spread in the responses between the types of observational products, with anomaly magnitudes and timings covering most of the behaviour seen in the models. The exception to this is the faster response of BCC-CSM, for which we do not find any observational evidence.

Whilst a horizontal resolution of 1° is relevant for evaluating ESMs, which represent an average coarse-scale behaviour of the Earth system, it is possible that the intraseasonal precipitation events and the vegetation responses do not spatially co-occur within this 1° grid box in observations. Therefore, to test whether the 1° GPP responses are attributable to the precipitation anomalies, we also composite the GPP response around intraseasonal wet events using the IMERG and VPM datasets at 0.25 and 0.1° horizontal resolution. The global composite GPP response is not found to be sensitive to spatial resolution (Fig. S1 in the Supplement). This indicates that the coarser 1° response, which represents the vegetation response at a scale relevant to ESMs, is representative of the processes occurring at much smaller spatial scales in the real world.

It is therefore clear that there is great uncertainty in the response of GPP to intraseasonal rainfall events in CMIP6 Earth system models but that the observations also fail to constrain this response. This makes it challenging to assess which of the model responses are most realistic from a global perspective. In order to further investigate whether the models are providing appropriate GPP responses, we therefore move to a regional evaluation.

3.2 Regional evaluation

To provide a regional assessment of GPP responses to intraseasonal rainfall events, we create composites for each IPCC AR6 land region (Iturbide et al., 2020) using the same method as in Sect. 3.1. This gives 46 regions, which are designed to represent areas with consistent climate features (Iturbide et al., 2020). Only 40 regions are included in this analysis: GIC (Greenland and Iceland), RAR (Russian Arctic), and the two Antarctic regions lie entirely outside the 60° S–60° N latitude band in which we identify intraseasonal precipitation events. We also remove the desert regions SAH (Sahara) and ARP (Arabian Peninsula) because these show outlying relationships between modelled and observed GPP anomalies, which is likely to be due to the very low GPP in these regions. All regions included in the analysis have a minimum of 500 precipitation events identified in each model and in observations. Full details of the sample sizes of events are included in Fig. S2.

In order to summarise the GPP responses in each region, we focus on three key properties of the composites, which are illustrated in Fig. 2a. The *peak amplitude* in GPP is defined as the maximum standardised anomaly occurring after the peak of the rainfall event composite (i.e. after day 0). The *lag* is the number of days after the rainfall peak that this peak amplitude occurs. The *post-event amplitude* is the mean standardised anomaly over days 40–60 after the rainfall peak, a period when there is no longer an anomaly in precipitation. The amplitude metrics characterise the contribution of intraseasonal wet events to GPP variability, while the lag measures how quickly GPP responds to a wet event.

Figure 2 compares the modelled peak amplitude, lag, and post-event amplitude of GPP in each AR6 region to values from one of the observation-based products. The observational product used for this comparison is FLUXCOM RS+METEO driven by CRU JRA v1 reanalysis (henceforth referred to as FLUXCOM-CRUJRAv1). This product is chosen as a starting point because FLUXCOM RS+METEO pro-

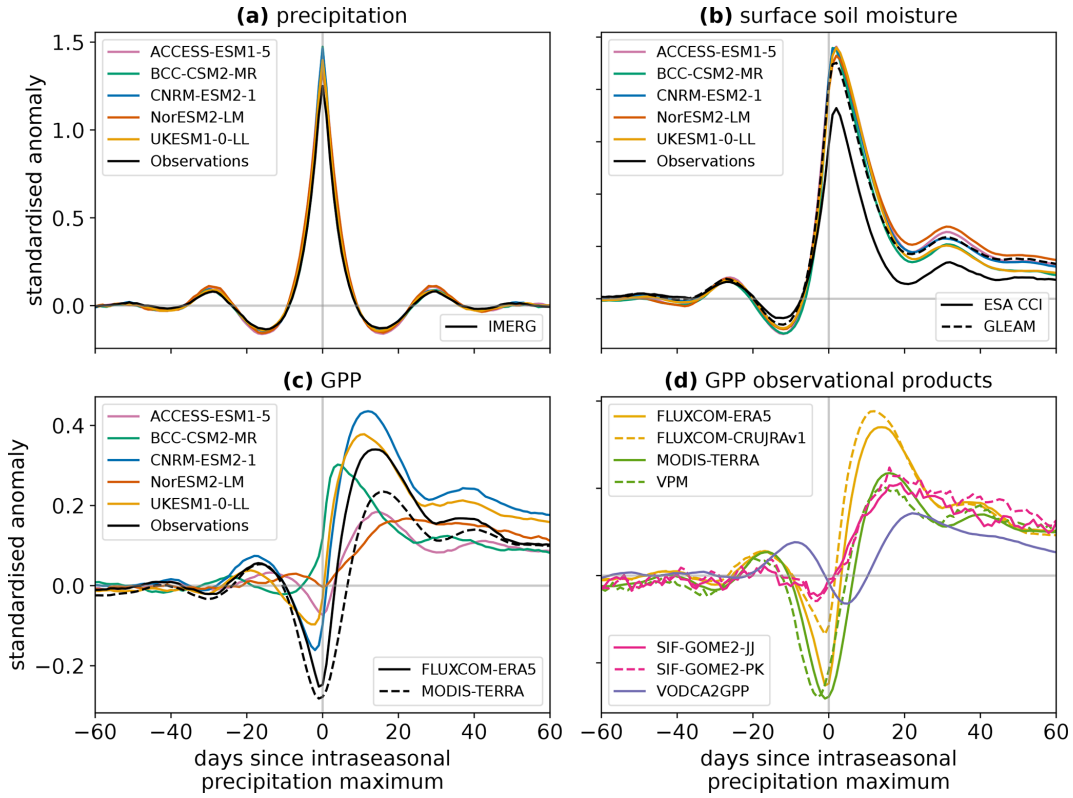

Figure 1. Composites of **(a)** precipitation, **(b)** surface soil moisture, and **(c, d)** GPP around intraseasonal wet events. All land pixels between 60° S and 60° N are included, except in months when the ground is frozen or in regions without valid ESA CCI Soil Moisture observations. The surface soil moisture and GPP composites have been scaled by the maximum amplitude of their corresponding precipitation composite.

vides the only available daily GPP data, but other observational products will be analysed later in this section. The peak and post-event amplitudes of GPP are scaled according to the observed peak and post-event amplitudes in surface soil moisture, respectively (i.e. the modelled peak amplitude in GPP is multiplied by the ratio between the observed and modelled peak amplitudes in surface soil moisture). Surface soil moisture is chosen as the scaling variable because the GPP amplitude is strongly linearly related to the surface soil moisture amplitude (see Fig. 4 and accompanying analysis later in the section). ESA CCI Soil Moisture is used as the benchmark observation. This scaling accounts for the possibility that individual models may under- or overestimate the regional surface soil moisture perturbation at the regional scale following wet events. Whilst a larger surface soil moisture perturbation is expected to lead to a larger-amplitude response in GPP, the scaled data allow us to assess the sensitivity of the GPP response to surface soil moisture by adjusting to identical surface soil moisture perturbations for each model.

All the analysed CMIP6 models show positive correlation for the peak and post-event amplitudes of regional GPP responses with FLUXCOM-CRUJRAv1, significant at the 95 % level (Fig. 2b and c, respectively). Importantly, this indicates that the models are generally able to correctly represent which regions develop larger anomalies in GPP following intraseasonal rainfall events. However, it is clear that the actual modelled values of response amplitude are very different between models. For example, in regions that show higher peak amplitudes in FLUXCOM-CRUJRAv1, UKESM is able to represent these higher amplitudes, whereas the amplitudes modelled by ACCESS-ESM and NorESM are much lower.

The lag of modelled regional GPP responses (Fig. 2d) is significantly correlated with observed lags for ACCESS-ESM, BCC-CSM, CNRM-ESM, and UKESM. No significant linear relationship is found between observed and modelled lags for NorESM, indicating that the timing of GPP responses to rainfall may not be realistic in this model. In many regions, the GPP lag modelled by NorESM is much longer (20–60 d) than the observed lag in any region. This suggests that the NorESM GPP response is generally too slow, which is consistent with this model showing the slowest response in the global composites in Fig. 1. Even for the models where a significant correlation in lag is found, the correlation coefficients are much lower than for the amplitude relationships, showing that the models match the observations better for the magnitude of the GPP response than the timing.

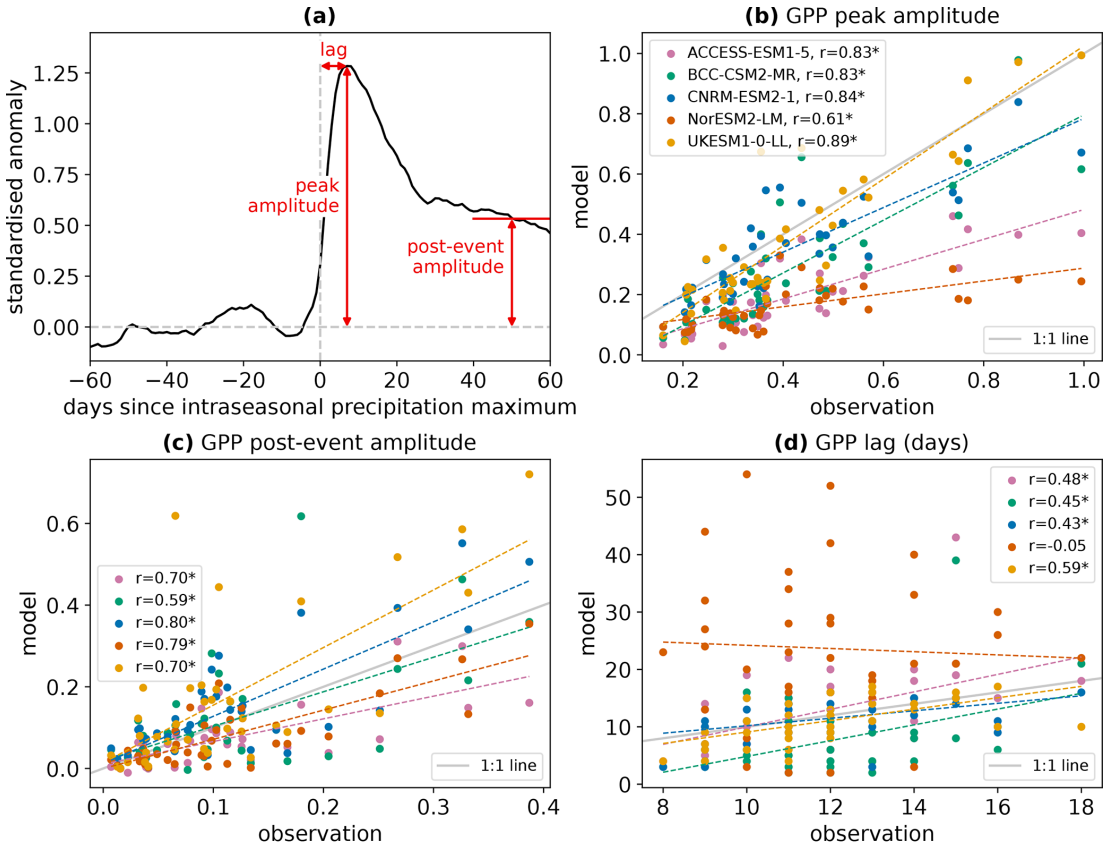

Figure 2. **(a)** Illustration of the three properties of the GPP response composite that will be analysed. The example composite used for the illustration is the GPP response from UKESM in the northern Australia region. **(b–d)** Comparison of the peak amplitude, post-event amplitude, and lag of the GPP response to intraseasonal wet events between the CMIP6 models and the FLUXCOM-CRUJRAv1 observational product. Each scatter point represents an AR6 region. Dashed lines show linear best fits and panel legends detail the linear correlation coefficients. Asterisks after correlation coefficients denote significance at the 95 % level. The grey lines indicate the identity line in each panel, i.e. where agreement between modelled and observed values would occur. The peak and post-event amplitudes in GPP have been scaled by the peak and post-event amplitudes in surface soil moisture, respectively.

Given the uncertainty in observed GPP responses established in Sect. 3.1, it is important to assess the effect of changing the observational GPP product on the results of the assessment carried out in Fig. 2. The Taylor diagrams presented in Fig. 3 show the correlation between regional responses for each possible model–observation pair, in addition to the inter-regional standard deviation normalised by the observed standard deviation $\left(\frac{\sigma_{\text{model}}}{\sigma_{\text{obs}}}\right)$ and the root mean squared error normalised by the observed standard deviation. For example, in Fig. 3a, the orange cross summarises the linear relationship between UKESM and FLUXCOM-CRUJRAv1 that is shown in full in Fig. 2b, which has a correlation of 0.89 and a slightly higher spread in peak GPP amplitudes between regions for the model than the observations $\left(\text{i.e. } \frac{\sigma_{\text{model}}}{\sigma_{\text{obs}}} \approx 1.2\right)$.

When focusing on the peak amplitude of the GPP response, the correlation between the model and observations shows some variation based on the choice of observational product, but the value typically lies between 0.8 and 0.9. The exception is NorESM, which is consistently a worse match for the observed regional distribution of GPP response amplitudes ($r \approx 0.6$), regardless of the observational product selected. The extent to which the inter-regional standard deviation in peak amplitudes matches the observed standard deviation is much more dependent on the choice of model than on the choice of observational product. This reflects the fact that some models produce much higher maximum regional peak amplitudes than others (as seen in Fig. 2). NorESM produces the lowest inter-regional variation in GPP response amplitudes, related to its inability to represent the larger responses; σ_{model} is far too low compared to the observed standard deviation, regardless of product. ACCESS-ESM also underestimates the inter-regional variation in response amplitudes compared to the observational products, while UKESM overestimates it. CNRM-ESM and BCC-CSM both reasonably capture the variation, falling within the spread of the observational products. Combined with their high correlation coeffi-

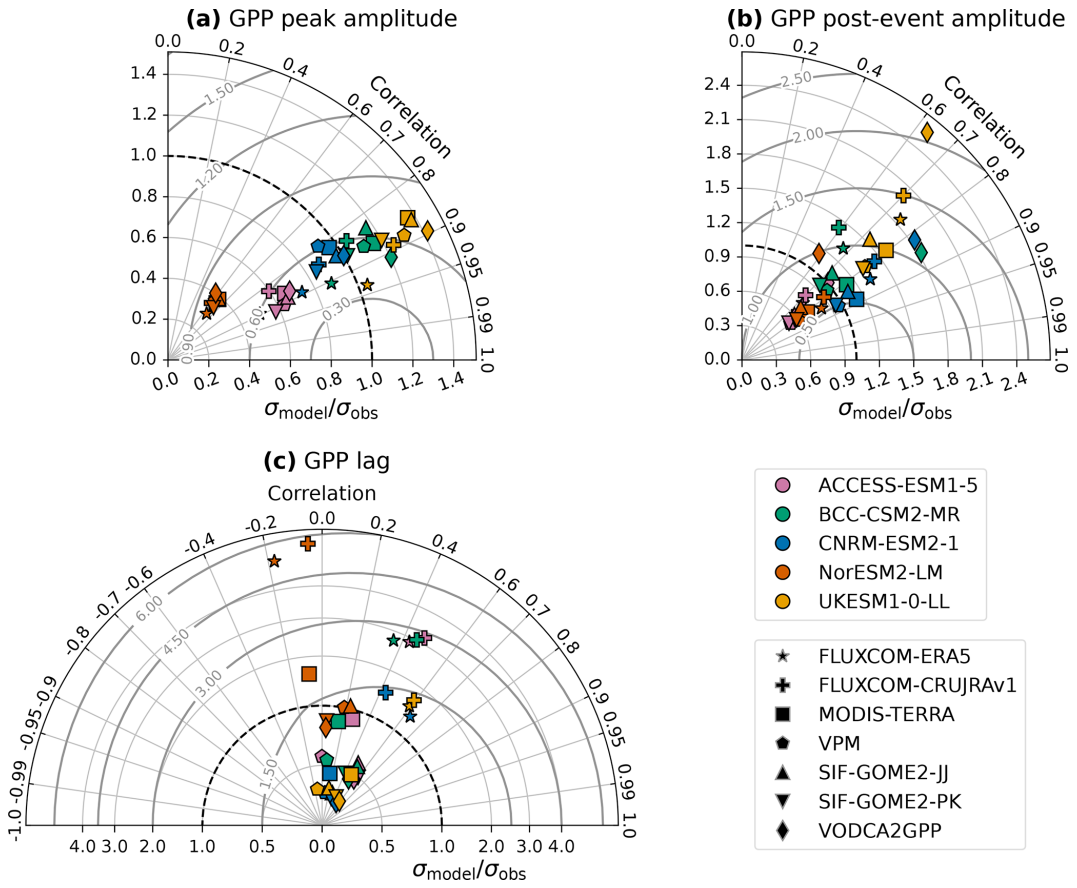

Figure 3. Taylor diagrams of regional relationships between modelled and observed GPP responses. Markers show the correlation and ratio of standard deviations $\frac{\sigma_{\text{model}}}{\sigma_{\text{obs}}}$ between the model and each observation-based GPP product for the **(a)** peak amplitude, **(b)** post-event amplitude, and **(c)** lag of the GPP response to intraseasonal wet events. The colour of the marker indicates which model is being evaluated, and the shape of the marker indicates the observation-based product used. The labelled grey contours indicate the root mean squared error normalised by observed standard deviation. GPP peak and post-event amplitudes have been scaled by the modelled peak and post-event amplitudes in surface soil moisture, respectively.

cients ($r > 0.8$), these two models therefore provide the most realistic representation of the differences between regions in the peak amplitude of GPP responses to intraseasonal rainfall events.

The correlation between models and observations is more dependent on the choice of observational product for the post-event amplitude (Fig. 3b – note the change in the radial axis scale from Fig. 3a) than for the peak amplitude. This indicates inter-product disagreement on which regions experience elevated GPP in the months following wet events. CNRM-ESM outperforms the other models here in terms of correlation and also produces a standard deviation consistent with several of the observational datasets. Similarly to the results for the peak amplitude, NorESM and ACCESS-ESM tend to underestimate the inter-regional variation in response, while UKESM overestimates it. In other words, intraseasonal rainfall events in NorESM and ACCESS-ESM play too minor a role in GPP variability compared to in observations.

Whereas all pairs of models and observations show correlations with $r > 0.5$ for both the peak and post-event amplitudes, the modelled lags in the regional GPP responses show much less agreement with the observed lags (Fig. 3c). Many of the relationships do not show a correlation significant at the 95 % level, with some even having a negative correlation. For each model, there are also large spreads in both the correlation and $\frac{\sigma_{\text{model}}}{\sigma_{\text{obs}}}$ dependent on the observations used for the assessment. The timing of GPP responses to intraseasonal rainfall events is much less well constrained by observations than the amplitude.

We now consider the possible causes of such large differences between models. Different inter-model GPP responses may arise due to differing land cover maps (e.g. if forests show a weaker response to rainfall events than other land cover, then a model with more extensive forest cover will produce a weaker globally composited GPP response). Alternatively, differences in the GPP response could be due to variations in the models' representation of processes linking

water availability and vegetation productivity so that changes in GPP differ between models even when identical land cover is being considered.

To assess whether the first possibility is solely responsible for the differing GPP responses seen in Fig. 1c, we compare regional land cover fractions between the models (Appendix A). We find that inter-model differences in the amplitude and lag of GPP responses can be seen even in regions where the models have similar land cover. Therefore, land cover differences cannot by themselves explain the discrepancies in the GPP response, so we further investigate the differences in water–carbon coupling processes. Two important processes that have known uncertainty in their representation in ESMs are the control of soil moisture stress on GPP and the response of stomatal conductance to changes in vapour pressure deficit (VPD). We therefore investigate the regional relationships between the GPP response and the perturbations in surface soil moisture (SSM) and near-surface VPD following the wet events.

Figure 4 explicitly compares these relationships in each model and in observations. Again, FLUXCOM-CRUJRAv1 is used as an illustrative observational GPP product, but the other products will be included later in the section to test the robustness of the relationships. ESA CCI Soil Moisture is used for the SSM observations, but the results are qualitatively unchanged if it is substituted with GLEAM (not shown). When defining the peak amplitude of the VPD response, the minimum rather than the maximum standardised anomaly is taken, since VPD typically decreases during and after intraseasonal wet events. Note that daily VPD data were not available for BCC-CSM, so this model is not included in the VPD analysis. SSM and VPD perturbations are not independent from one another; the regional amplitudes of SSM and VPD responses are strongly negatively correlated (not shown). However, we test the relationship of GPP with both variables since they influence the GPP through different modelled processes.

All models represent the observed positive correlation between the SSM peak amplitude and the GPP peak amplitude: regions with a larger standardised anomaly in SSM following rainfall events show a larger standardised anomaly in GPP due to the greater change in water availability. The models also capture the observed negative correlation between the peak amplitudes of the VPD and GPP responses. Regions with a smaller drop in VPD standardised anomaly after wet events are experiencing less evaporative demand compared to climatological conditions, so stomata can remain open to allow photosynthesis without experiencing as much water loss to the atmosphere. These correlations are significant ($p < 0.05$) in all the observational products tested (Fig. S4a and b). However, even though all models represent these basic relationships, there are large differences between the correlation coefficients, meaning that GPP responses to rainfall are more tightly coupled to the associated perturbations in SSM and VPD in some models than others. For example, in CNRM-ESM2-1, the correlation between the peak amplitude of the SSM perturbations and the peak amplitude of the GPP response is $r = 0.94$, meaning that the magnitude of the SSM perturbations can explain 89 % of the variance in the GPP peak amplitude between regions ($r^2 = 0.89$), whereas in UKESM1-0-LL it only explains 52 % of the variance ($r = 0.72$, $r^2 = 0.52$).

There are also differences between models in the slopes of the linear relationships. This demonstrates that the models' GPP peak amplitudes have varying sensitivities to changes in the peak amplitude of the SSM and VPD perturbations. For example, for a given increase in the peak standardised anomaly of SSM, NorESM exhibits a much smaller increase in the associated GPP peak anomaly than the other models. We test the significance of these differences in sensitivity among all the models and all the observational GPP products. This is done using estimated marginal means of linear trends and correcting for multiple testing using the Tukey method. Figure 5 shows the resulting 95 % confidence intervals for the sensitivity of the GPP responses to the driving perturbations in SSM and VPD. This analysis shows that for the relationship between the peak amplitudes of VPD and GPP (Fig. 5b), the sensitivity of NorESM is significantly different ($p < 0.1$) to the sensitivity of all other models and all observational GPP products except SIF-GOME2-JJ. These differences are also all significant at $p < 0.05$ other than NorESM-VODCA2GPP. Therefore, we conclude that the amplitude of GPP responses to wet events in NorESM is not sufficiently sensitive to the changes in vapour pressure deficit.

The peak amplitude of GPP responses is also less sensitive to SSM perturbations in NorESM than in the other models (Fig. 5a), showing a significantly ($p < 0.05$) different sensitivity to BCC-CSM, CNRM-ESM, and UKESM. However, of the seven observational products, the SSM sensitivity in NorESM is only significantly different to FLUXCOM-ERA5, so there is insufficient evidence here to state that it is unrealistic compared to the range of observations. In contrast, the peak amplitude of GPP responses in BCC-CSM shows excessive sensitivity to SSM perturbations, with significant ($p < 0.05$) differences to MODIS Terra, VPM, SIF-GOME2-JJ, and VODCA2GPP (and $p < 0.1$ for the difference with FLUXCOM-CRUJRAv1). It additionally shows a significantly higher sensitivity than two of the other models (NorESM and ACCESS-ESM).

Similar relationships between SSM and VPD as well as GPP are also found for the post-event amplitudes, but the correlation is generally weaker than for the peak amplitudes. The peak amplitude of GPP is more strongly constrained by the concurrent SSM and VPD anomalies than the post-event amplitude. In the case of NorESM, the correlation is sufficiently weak that no significant relationship is found between SSM and GPP amplitudes after the event when testing at the 95 % level; vegetation productivity is much less strongly linked to surface soil water conditions than in the other models and in the observations (again, the correlations

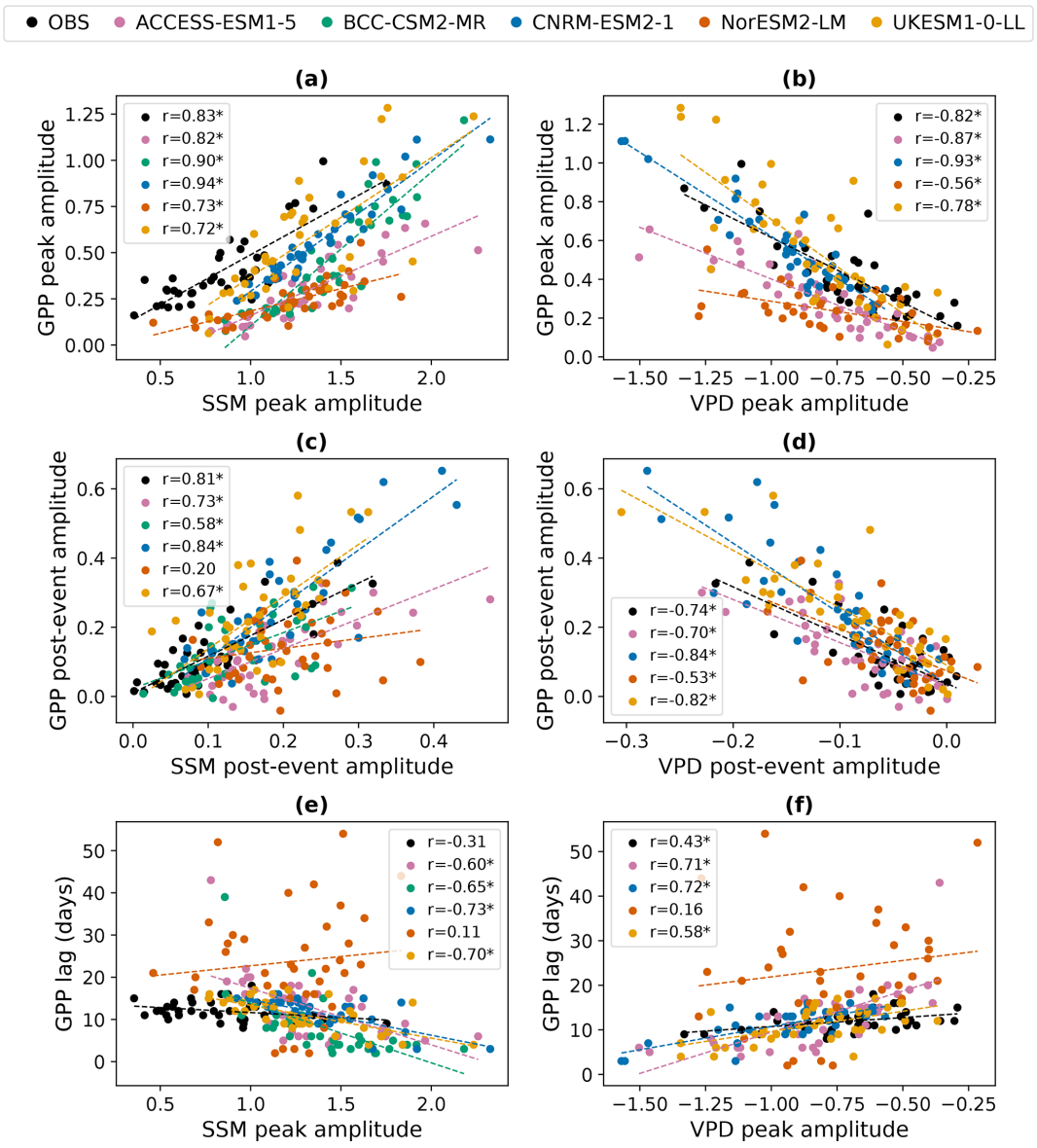

Figure 4. Regional GPP responses to intraseasonal wet events compared to the driving perturbations in surface soil moisture (SSM: **a, c, e**) and vapour pressure deficit (VPD: **b, d, f**). Each scatter point represents an IPCC AR6 region. Dashed lines show linear best fits. The legend for each panel indicates the linear correlation coefficient between the driving perturbation and the GPP response for each model. Asterisks after correlation coefficients denote significance at the 95 % level. The uppermost legend, showing which model is denoted by each colour, applies to all panels. The observational products (OBS) used are FLUXCOM-CRUJRAv1 (GPP), ESA CCI (surface soil moisture), and ERA5 (VPD).

are significant at $p < 0.05$ in all the observational products tested). The weaker relationships between post-event amplitudes can be partly explained by the fact that over the 40–60 d timescale, changes in root zone soil moisture explain more of the variation in the GPP amplitudes than changes only in the surface layer (whereas the surface layer is generally more important for the peak amplitude). Comparing the post-event amplitude of soil moisture in the top 1 m of soil with the post-event amplitude of GPP gives higher correlation coefficients than seen in Fig. 4c for all models (other than BCC-CSM, for which the 1 m layer data are not available), as shown in Fig. S5. In the months after the peak of the wet event, the rainfall infiltrates the soil and provides additional moisture availability to vegetation at deeper soil levels. Figures 4c and 5c show that NorESM is less sensitive to the SSM post-event amplitude than the other models, although its sensitivity is significantly ($p < 0.05$) different only to UKESM, CNRM-ESM, and four out of the seven observational products. The modelled sensitivity to VPD post-event amplitude is not inconsistent with observations for any model.

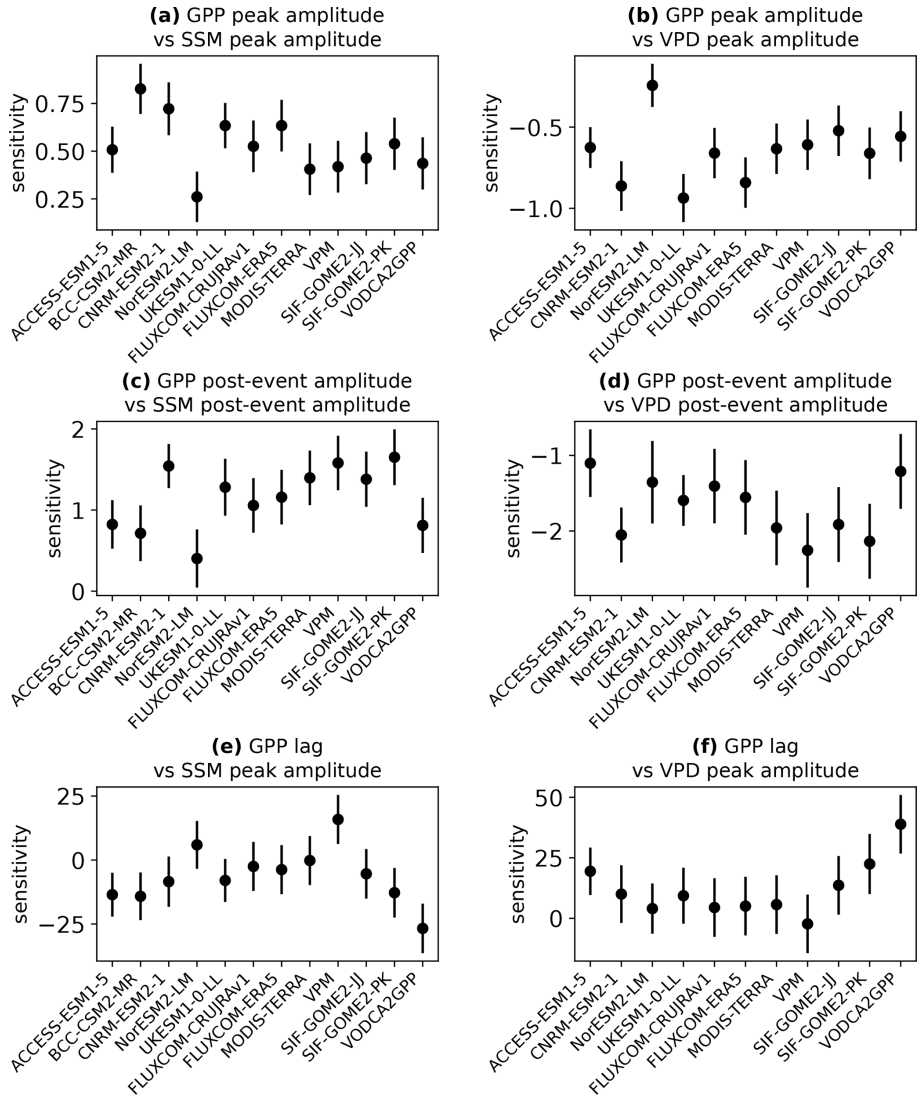

Figure 5. Sensitivity of regional GPP responses to intraseasonal wet events compared to the driving perturbations in surface soil moisture **(a, c, e)** and VPD **(b, d, f)**. Error bars denote 95 % confidence intervals. The sensitivity of the observational GPP products is measured with respect to ESA CCI for surface soil moisture and ERA5 for VPD.

The lag in GPP response is compared to the peak amplitude rather than the lag of SSM and VPD because there is very little variation in SSM and VPD lags between regions due to these variables responding very quickly (1–3 d) after rainfall. In the models, the lag of the GPP response tends to be shorter in regions with larger perturbations in SSM and VPD. All models exhibit this relationship except NorESM. However, the evidence for the relationship in the observations is much weaker (see Fig. S4). Only two of the seven observational products tested show a significant ($p < 0.05$) negative correlation between SSM peak amplitude and GPP lag (FLUXCOM-ERA5 and VODCA2GPP), while VPM shows a significant positive correlation. Four out of the seven products show a significant positive correlation between VPD peak amplitude and GPP lag (FLUXCOM-ERA5, FLUXCOM-CRUJRAv1, SIF-GOME2-PK, and VODCA2GPP). Even in the observational products that do show these significant relationships, the correlation coefficients are much lower than those obtained from the models. The highest correlation coefficients from observations are from VODCA2GPP at $r = -0.50$ for the correlation between SSM peak amplitude and GPP lag and $r = 0.56$ for VPD peak amplitude and GPP lag. These correlations are considerably weaker than those found in the models (other than NorESM), which have $|r|$ between 0.58 and 0.73. It is therefore possible that the timing of the GPP responses in the models is too tightly constrained by the amplitude of the regional perturbations in SSM and VPD.

4 Discussion and conclusions

This work has demonstrated that the responses of vegetation productivity to intraseasonal rainfall events are very different between ESMs participating in CMIP6. Of the models tested, UKESM and CNRM-ESM tend to produce larger standardised anomalies of GPP following rainfall events, while ACCESS-ESM and NorESM produce smaller productivity anomalies. There are also differences in the timing of the models' responses following the rainfall events, with NorESM taking much longer to reach its peak GPP anomaly and BCC-CSM responding most quickly. The models all correctly represent larger anomalies in regional GPP being associated with larger increases in surface soil moisture and larger decreases in near-surface vapour pressure deficit. However, the strength of these relationships and the sensitivity of the GPP responses to these drivers vary between models. In particular, GPP responses in BCC-CSM show excessive sensitivity to intraseasonal surface soil moisture perturbations, while NorESM is not sufficiently sensitive to vapour pressure deficit perturbations. This aligns with the findings of Anav et al. (2015) that NorESM has lower seasonal and interannual variability than other models.

The reasons for this diversity in model behaviour are likely multiple and complex. We suggest that unravelling them requires in-depth knowledge of each model configuration, parameterisation structure, and parameter values, which is beyond the scope of this paper. Likely causes include differences in the soil moisture stress function applied to downregulate GPP and in the stomatal conductance models, which control how changes in VPD affect GPP, as discussed in Sect. 1. Further work should therefore compare the GPP responses between different versions of particular ESMs or land surface models to establish how specific changes in configuration – for example, alternative soil moisture stress parameters and stomatal conductance models – impact the coupling between water availability and vegetation productivity. The vertical profile of root water uptake may also play a role. Each model discretises the soil column into layers differently and prescribes different root depths for plant functional types. In a model where vegetation is able to access deeper reserves of soil water, it may become less water-stressed and therefore exhibit smaller responses to rainfall events. Additionally, the partitioning of rainfall into direct evaporation, transpiration, and runoff, which operate on different timescales, will impact the magnitude and timing of water availability for vegetation following a rainfall event. The post-rainfall GPP response could also be affected by each model's representation of drought deciduous phenology (for example, drought deciduous phenology is turned off in UKESM).

Further work is therefore needed to understand why different methods for deriving global GPP products result in different relationships with water availability, quantify the uncertainty in these products, and ultimately obtain observations that will reduce our uncertainty in the response of GPP to intraseasonal rainfall events. Some of the issue with timing in the observations may be due to the 8-daily temporal resolution of all products other than FLUXCOM RS+METEO. We therefore emphasise the usefulness of GPP data at the daily timescale for diagnostics of climate–carbon cycle coupling. Many models only make GPP data from CMIP experiments publicly available at monthly resolution. Future prioritisation of sub-monthly vegetation data would aid the investigation of process-oriented diagnostics that can help us understand land–atmosphere coupling in these models. Insights at this timescale are key for constraining model processes, and in many regions the response of vegetation productivity to events on this timescale is important for determining its annual mean (e.g. Wu et al., 2021). Daily SIF observations could be a valuable resource for understanding GPP responses to rainfall events, particularly since they are less affected by cloud cover than alternative vegetation observations such as the normalised difference vegetation index (NDVI).

This study has demonstrated a framework for evaluating an important link between the water and carbon cycles in ESMs by assessing the response of GPP to intraseasonal rainfall events. In the recent historical period of CMIP6 simulations, models show diverse behaviour in their GPP responses, and only some aspects of this can be constrained by the currently available observations. It is therefore difficult to determine which models represent the most realistic vegetation responses to wet conditions. This means it is challenging to understand and model the behaviour of the land carbon sink and its consequences for atmospheric CO_2 levels in the present day and to have confidence that the sink is represented correctly in projections under future scenarios. Improvements are required in both our understanding of how model configurations and parameters affect the resulting vegetation productivity responses to water availability and the observational datasets used to evaluate this coupling.

Appendix A

Inter-model differences in the GPP responses to water availability could arise due to the presence of discrepancies in the models' land cover maps. For example, if one model represents a higher percentage of forested land in a region, its GPP is likely to show less of a response to intraseasonal rainfall events in this region than a model with higher grassland coverage.

To demonstrate that differences in GPP responses between models occur even where the land cover distributions are similar, Fig. A1 shows the land cover distributions and the responses of SSM, VPD, and GPP to intraseasonal rainfall events (as in the global composites of Fig. 1) for the IPCC AR6 Central North America (CNA) region (Iturbide et al., 2020). The mean land cover over the period 2000–2014 is

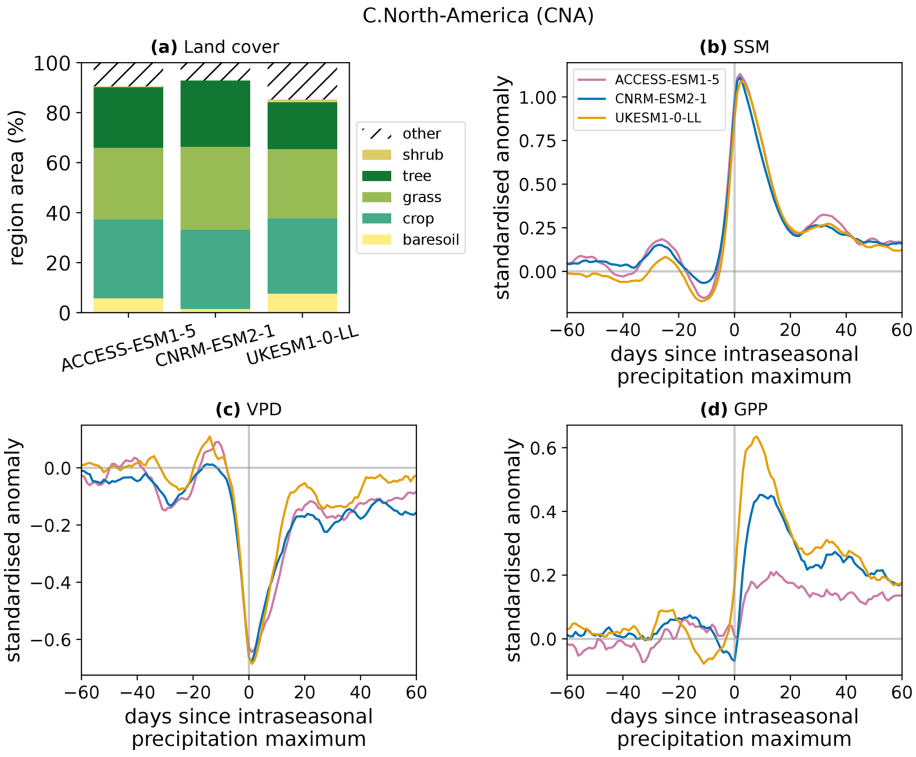

Figure A1. Land cover and responses to intraseasonal wet events in the Central North America (CNA) AR6 region. **(a)** Percentage of the region assigned to each land cover. The "other" category includes water bodies. **(b–d)** Responses of standardised anomalies in surface soil moisture **(b)**, near-surface vapour pressure deficit **(c)**, and GPP **(d)** in the three models that provide land cover information. These composites have been scaled by the maximum of the precipitation composite for each model.

used for Fig. A1a. Only three models are included: land cover data were not available for BCC-CSM2-MR or NorESM2-LM.

All three models have similar land cover in this region. ACCESS-ESM and UKESM are the most alike, with CNRM-ESM having a lower fraction of bare soil and more vegetated cover. However, this higher similarity between the land cover of ACCESS-ESM and UKESM does not translate into greater agreement in their responses of GPP to rainfall. Although the models produce consistent responses in SSM and VPD, the GPP responses are very different, as was found in the global evaluation of Sect. 3.1. The peak standardised anomaly in GPP following rainfall events in this region is approximately 3 times higher in UKESM than in ACCESS-ESM. Since in this case we have established that the difference is not due to a disparity in the land cover distribution, we conclude that it is the result of differences in the models' representations of water–vegetation coupling processes.

Code and data availability. Daily GPP data from FLUXCOM RS+METEO are available on request from the FLUXCOM team (see http://www.fluxcom.org/CF-Download/ for details). All other datasets used in this paper are publicly available for download. CMIP6 model data: https://doi.org/10.22033/ESGF/CMIP6.4003 (Seferian, 2019), https://doi.org/10.22033/ESGF/CMIP6.7924 (Seland et al., 2019), https://doi.org/10.22033/ESGF/CMIP6.5929 (Tang et al., 2019), https://doi.org/10.22033/ESGF/CMIP6.2901 (Wu et al., 2018), https://doi.org/10.22033/ESGF/CMIP6.4242 (Ziehn et al., 2019). ERA5: https://doi.org/10.24381/cds.adbb2d47 (Hersbach et al., 2023). IMERG precipitation: https://doi.org/10.5067/GPM/IMERGDF/DAY/06 (Huffman et al., 2019). ESA CCI Soil Moisture combined product v06.1: https://catalogue.ceda.ac.uk/uuid/43d73291472444e6b9c2d2420dbad7d6 (Dorigo et al., 2021) (last access: 23 July 2021). GLEAM v3.6a soil moisture: https://www.gleam.eu/#downloads (last access: 16 December 2022). MODIS Terra GPP aggregated to 0.5° resolution: https://doi.org/10.25592/uhhfdm.8556 (Kern, 2021). VPM GPP (8-daily at 0.5° resolution): https://doi.org/10.6084/m9.figshare.c.3789814.v1 (Zhang et al., 2017b). Downscaled GOME-2 SIF: https://doi.org/10.2905/21935FFC-B797-4BEE-94DA-8FEC85B3F9E1 (Duveiller et al., 2020). VODCA2GPP: https://doi.org/10.48436/1k7aj-bdz35 (Wild et al., 2021). The code used to generate the results and figures in this paper is available at https://doi.org/10.5281/zenodo.11263264 (Harris, 2024).

Supplement. The supplement related to this article is available online at: https://doi.org/10.5194/esd-15-1019-2024-supplement.

Author contributions. BLH: conceptualisation, data curation, formal analysis, investigation, methodology, software, visualisation, writing (original draft preparation; review and editing). TQ: funding acquisition, writing (original draft preparation; review and editing). CMT: conceptualisation, funding acquisition, supervision, project administration, writing (review and editing). PPH: methodology, writing (review and editing).

Competing interests. The contact author has declared that none of the authors has any competing interests.

Disclaimer. Publisher's note: Copernicus Publications remains neutral with regard to jurisdictional claims made in the text, published maps, institutional affiliations, or any other geographical representation in this paper. While Copernicus Publications makes every effort to include appropriate place names, the final responsibility lies with the authors.

Acknowledgements. We acknowledge the World Climate Research Programme, which, through its Working Group on Coupled Modelling, coordinated and promoted CMIP6. We thank the climate modelling groups for producing and making available their model output, the Earth System Grid Federation (ESGF) for archiving the data and providing access, and the multiple funding agencies who support CMIP6 and ESGF. We thank the FLUXCOM team for making the daily GPP data from FLUXCOM RS+METEO available to us. The figures were designed using the colourblind-safe colour scheme provided by Wong (2011). The Taylor diagrams in Fig. 3 were produced using an adaptation of code from Copin (2012). We thank two anonymous reviewers for their feedback, which helped to clarify and improve the manuscript.

Financial support. This study was funded as part of the Natural Environment Research Council's support of the National Centre for Earth Observation via the projects CPEO (Constraining Coupled Carbon and Water Cycle Processes with Earth Observation; grant no. NE/X006328/1) and TerraFIRMA (Future Impacts, Risks and Mitigation Actions in a changing Earth system; grant no. NE/W004895/1). Bethan L. Harris also received funding through a European Space Agency Climate Change Initiative (ESA CCI) fellowship.

Review statement. This paper was edited by Anping Chen and reviewed by two anonymous referees.

References

Alemohammad, S. H., Fang, B., Konings, A. G., Aires, F., Green, J. K., Kolassa, J., Miralles, D., Prigent, C., and Gentine, P.: Water, Energy, and Carbon with Artificial Neural Networks (WECANN): a statistically based estimate of global surface turbulent fluxes and gross primary productivity using solar-induced fluorescence, Biogeosciences, 14, 4101–4124, https://doi.org/10.5194/bg-14-4101-2017, 2017.

Anav, A., Friedlingstein, P., Beer, C., Ciais, P., Harper, A., Jones, C., Murray-Tortarolo, G., Papale, D., Parazoo, N. C., Peylin, P., Piao, S., Sitch, S., Viovy, N., Wiltshire, A., and Zhao, M.: Spatiotemporal patterns of terrestrial gross primary production: A review, Rev. Geophys., 53, 785–818, https://doi.org/10.1002/2015RG000483, 2015.

Bai, J., Zhang, H., Sun, R., Li, X., Xiao, J., and Wang, Y.: Estimation of global GPP from GOME-2 and OCO-2 SIF by considering the dynamic variations of GPP-SIF relationship, Agr. Forest Meteorol., 326, 109180, https://doi.org/10.1016/J.AGRFORMET.2022.109180, 2022.

Ball, J. T., Woodrow, I. E., and Berry, J. A.: A Model Predicting Stomatal Conductance and its Contribution to the Control of Photosynthesis under Different Environmental Conditions, in: Progress in Photosynthesis Research: Vol. 4, Proceedings of the VIIth International Congress on Photosynthesis Providence, Rhode Island, USA, 10–15 August 1986, edited by: Biggins, J., Springer Netherlands, Dordrecht, 221–224, https://doi.org/10.1007/978-94-017-0519-6_48, 1987.

Barnes, M. L., Farella, M. M., Scott, R. L., Moore, D. J., Ponce-Campos, G. E., Biederman, J. A., MacBean, N., Litvak, M. E., and Breshears, D. D.: Improved dryland carbon flux predictions with explicit consideration of water-carbon coupling, Communications Earth & Environment, 2, 1–9, https://doi.org/10.1038/s43247-021-00308-2, 2021.

Beck, H. E., van Dijk, A. I. J. M., Levizzani, V., Schellekens, J., Miralles, D. G., Martens, B., and de Roo, A.: MSWEP: 3-hourly 0.25° global gridded precipitation (1979–2015) by merging gauge, satellite, and reanalysis data, Hydrol. Earth Syst. Sci., 21, 589–615, https://doi.org/10.5194/hess-21-589-2017, 2017.

Bolton, D.: The Computation of Equivalent Potential Temperature, Mon. Weather Rev., 108, 1046–1053, https://doi.org/10.1175/1520-0493(1980)108%3C1046:TCOEPT%3E2.0.CO;2, 1980.

Bonan, G. B., Williams, M., Fisher, R. A., and Oleson, K. W.: Modeling stomatal conductance in the earth system: linking leaf water-use efficiency and water transport along the soil–plant–atmosphere continuum, Geosci. Model Dev., 7, 2193–2222, https://doi.org/10.5194/gmd-7-2193-2014, 2014.

Canadell, J., Monteiro, P., Costa, M., Cotrim da Cunha, L., Cox, P., Eliseev, A., Henson, S., Ishii, M., Jaccard, S., Koven, C., Lohila, A., Patra, P., Piao, S., Rogelj, J., Syampungani, S., Zaehle, S., and Zickfeld, K.: Global Carbon and other Biogeochemical Cycles and Feedbacks, in: Climate Change 2021: The Physical Science Basis. Contribution of Working Group I to the Sixth Assessment Report of the Intergovernmental Panel on Climate Change, edited by: Masson-Delmotte, V., Zhai, P., Pirani, A., Connors, S., Péan, C., Berger, S., Caud, N., Chen, Y., Goldfarb, L., Gomis, M., Huang, M., Leitzell, K., Lonnoy, E., Matthews, J., Maycock, T., Waterfield, T., Yelekçi, O., Yu, R., and Zhou, B., Cambridge University Press, Cambridge, United Kingdom and New York, NY, USA, 673–816, https://doi.org/10.1017/9781009157896.007, 2021.

Chen, A., Mao, J., Ricciuto, D., Lu, D., Xiao, J., Li, X., Thornton, P. E., and Knapp, A. K.: Seasonal changes in GPP/SIF ratios and their climatic determinants across the

Northern Hemisphere, Global Change Biol., 27, 5186–5197, https://doi.org/10.1111/GCB.15775, 2021.

Chen, C., Riley, W. J., Prentice, I. C., and Keenan, T. F.: CO_2 fertilization of terrestrial photosynthesis inferred from site to global scales, P. Natl. Acad. Sci. USA, 119, e2115627119, https://doi.org/10.1073/pnas.2115627119, 2022.

Copin, Y.: Taylor diagram for python/matplotlib (2018-12-06) [code], https://doi.org/10.5281/zenodo.5548061, 2012.

Dorigo, W., Wagner, W., Albergel, C., Albrecht, F., Balsamo, G., Brocca, L., Chung, D., Ertl, M., Forkel, M., Gruber, A., Haas, E., Hamer, P. D., Hirschi, M., Ikonen, J., de Jeu, R., Kidd, R., Lahoz, W., Liu, Y. Y., Miralles, D., Mistelbauer, T., Nicolai-Shaw, N., Parinussa, R., Pratola, C., Reimer, C., van der Schalie, R., Seneviratne, S. I., Smolander, T., and Lecomte, P.: ESA CCI Soil Moisture for improved Earth system understanding: State-of-the art and future directions, Remote Sens. Environ., 203, 185–215, https://doi.org/10.1016/J.RSE.2017.07.001, 2017.

Dorigo, W., Preimesberger, W., Moesinger, L., Pasik, A., Scanlon, T., Hahn, S., Van der Schalie, R., Van der Vliet, M., De Jeu, R., Kidd, R., Rodriguez-Fernandez, N., and Hirschi, M.: ESA Soil Moisture Climate Change Initiative (Soil_Moisture_cci): COMBINED product, Version 06.1, NERC EDS Centre for Environmental Data Analysis [data set], https://catalogue.ceda.ac.uk/uuid/43d73291472444e6b9c2d2420dbad7d6, 2021.

Duveiller, G., Frankenberg, C., Filipponi, F., Walther, S., Köhler, P., Guanter, L., and Cescatti, A.: Downscaled GOME2 SIF. European Commission, Joint Research Centre (JRC) [data set], https://doi.org/10.2905/21935FFC-B797-4BEE-94DA-8FEC85B3F9E1, 2019.

Duveiller, G., Filipponi, F., Walther, S., Köhler, P., Frankenberg, C., Guanter, L., and Cescatti, A.: A spatially downscaled sun-induced fluorescence global product for enhanced monitoring of vegetation productivity, Earth Syst. Sci. Data, 12, 1101–1116, https://doi.org/10.5194/essd-12-1101-2020, 2020.

Eyring, V., Bony, S., Meehl, G. A., Senior, C. A., Stevens, B., Stouffer, R. J., and Taylor, K. E.: Overview of the Coupled Model Intercomparison Project Phase 6 (CMIP6) experimental design and organization, Geosci. Model Dev., 9, 1937–1958, https://doi.org/10.5194/gmd-9-1937-2016, 2016.

Fernández-Martínez, M., Vicca, S., Janssens, I. A., Sardans, J., Luyssaert, S., Campioli, M., Chapin, F. S., Ciais, P., Malhi, Y., Obersteiner, M., Papale, D., Piao, S. L., Reichstein, M., Rodà, F., and Peñuelas, J.: Nutrient availability as the key regulator of global forest carbon balance, Nat. Clim. Change, 4, 471–476, https://doi.org/10.1038/nclimate2177, 2014.

Frankenberg, C., Fisher, J. B., Worden, J., Badgley, G., Saatchi, S. S., Lee, J.-E., Toon, G. C., Butz, A., Jung, M., Kuze, A., and Yokota, T.: New global observations of the terrestrial carbon cycle from GOSAT: Patterns of plant fluorescence with gross primary productivity, Geophys. Res. Lett., 38, L17706, https://doi.org/10.1029/2011GL048738, 2011.

Friedlingstein, P., O'Sullivan, M., Jones, M. W., Andrew, R. M., Gregor, L., Hauck, J., Le Quéré, C., Luijkx, I. T., Olsen, A., Peters, G. P., Peters, W., Pongratz, J., Schwingshackl, C., Sitch, S., Canadell, J. G., Ciais, P., Jackson, R. B., Alin, S. R., Alkama, R., Arneth, A., Arora, V. K., Bates, N. R., Becker, M., Bellouin, N., Bittig, H. C., Bopp, L., Chevallier, F., Chini, L. P., Cronin, M., Evans, W., Falk, S., Feely, R. A., Gasser, T., Gehlen, M., Gkritzalis, T., Gloege, L., Grassi, G., Gruber, N., Gürses, Ö., Harris, I., Hefner, M., Houghton, R. A., Hurtt, G. C., Iida, Y., Ilyina, T., Jain, A. K., Jersild, A., Kadono, K., Kato, E., Kennedy, D., Klein Goldewijk, K., Knauer, J., Korsbakken, J. I., Landschützer, P., Lefèvre, N., Lindsay, K., Liu, J., Liu, Z., Marland, G., Mayot, N., McGrath, M. J., Metzl, N., Monacci, N. M., Munro, D. R., Nakaoka, S.-I., Niwa, Y., O'Brien, K., Ono, T., Palmer, P. I., Pan, N., Pierrot, D., Pocock, K., Poulter, B., Resplandy, L., Robertson, E., Rödenbeck, C., Rodriguez, C., Rosan, T. M., Schwinger, J., Séférian, R., Shutler, J. D., Skjelvan, I., Steinhoff, T., Sun, Q., Sutton, A. J., Sweeney, C., Takao, S., Tanhua, T., Tans, P. P., Tian, X., Tian, H., Tilbrook, B., Tsujino, H., Tubiello, F., van der Werf, G. R., Walker, A. P., Wanninkhof, R., Whitehead, C., Willstrand Wranne, A., Wright, R., Yuan, W., Yue, C., Yue, X., Zaehle, S., Zeng, J., and Zheng, B.: Global Carbon Budget 2022, Earth Syst. Sci. Data, 14, 4811–4900, https://doi.org/10.5194/essd-14-4811-2022, 2022.

Grossiord, C., Buckley, T. N., Cernusak, L. A., Novick, K. A., Poulter, B., Siegwolf, R. T., Sperry, J. S., and McDowell, N. G.: Plant responses to rising vapor pressure deficit, New Phytol., 226, 1550–1566, https://doi.org/10.1111/nph.16485, 2020.

Gruber, A., Scanlon, T., van der Schalie, R., Wagner, W., and Dorigo, W.: Evolution of the ESA CCI Soil Moisture climate data records and their underlying merging methodology, Earth Syst. Sci. Data, 11, 717–739, https://doi.org/10.5194/essd-11-717-2019, 2019.

Guan, K., Good, S. P., Caylor, K. K., Sato, H., Wood, E. F., and Li, H.: Continental-scale impacts of intra-seasonal rainfall variability on simulated ecosystem responses in Africa, Biogeosciences, 11, 6939–6954, https://doi.org/10.5194/bg-11-6939-2014, 2014.

Guan, K., Good, S. P., Caylor, K. K., Medvigy, D., Pan, M., Wood, E. F., Sato, H., Biasutti, M., Chen, M., Ahlström, A., and Xu, X.: Simulated sensitivity of African terrestrial ecosystem photosynthesis to rainfall frequency, intensity, and rainy season length, Environ. Res. Lett., 13, 025013, https://doi.org/10.1088/1748-9326/AA9F30, 2018.

Harper, A. B., Williams, K. E., McGuire, P. C., Duran Rojas, M. C., Hemming, D., Verhoef, A., Huntingford, C., Rowland, L., Marthews, T., Breder Eller, C., Mathison, C., Nobrega, R. L. B., Gedney, N., Vidale, P. L., Otu-Larbi, F., Pandey, D., Garrigues, S., Wright, A., Slevin, D., De Kauwe, M. G., Blyth, E., Ardö, J., Black, A., Bonal, D., Buchmann, N., Burban, B., Fuchs, K., de Grandcourt, A., Mammarella, I., Merbold, L., Montagnani, L., Nouvellon, Y., Restrepo-Coupe, N., and Wohlfahrt, G.: Improvement of modeling plant responses to low soil moisture in JULESvn4.9 and evaluation against flux tower measurements, Geosci. Model Dev., 14, 3269–3294, https://doi.org/10.5194/gmd-14-3269-2021, 2021.

Harris, B. L.: cmip6-gpp-isv: v2.0 (v2.0), Zenodo [code], https://doi.org/10.5281/zenodo.11263264, 2024.

Harris, B. L., Taylor, C. M., Weedon, G. P., Talib, J., Dorigo, W., and van der Schalie, R.: Satellite-Observed Vegetation Responses to Intraseasonal Precipitation Variability, Geophys. Res. Lett., 49, e2022GL099635, https://doi.org/10.1029/2022GL099635, 2022.

Harris, I.: A forcings dataset of gridded land surface blend of Climatic Research Unit (CRU) and Japanese reanalysis (JRA) data; Jan. 1901–Dec. 2017, https://doi.org/10.5285/13f3635174794bb98cf8ac4b0ee8f4ed, 2019.

Harris, I., Jones, P. D., Osborn, T. J., and Lister, D. H.: Updated high-resolution grids of monthly climatic observations – the CRU TS3.10 Dataset, Int. J. Climatol., 34, 623–642, https://doi.org/10.1002/JOC.3711, 2014.

Hersbach, H., Bell, B., Berrisford, P., Hirahara, S., Horányi, A., Muñoz-Sabater, J., Nicolas, J., Peubey, C., Radu, R., Schepers, D., Simmons, A., Soci, C., Abdalla, S., Abellan, X., Balsamo, G., Bechtold, P., Biavati, G., Bidlot, J., Bonavita, M., De Chiara, G., Dahlgren, P., Dee, D., Diamantakis, M., Dragani, R., Flemming, J., Forbes, R., Fuentes, M., Geer, A., Haimberger, L., Healy, S., Hogan, R. J., Hólm, E., Janisková, M., Keeley, S., Laloyaux, P., Lopez, P., Lupu, C., Radnoti, G., de Rosnay, P., Rozum, I., Vamborg, F., Villaume, S., and Thépaut, J. N.: The ERA5 global reanalysis, Q. J. Roy. Meteor. Soc., 146, 1999–2049, https://doi.org/10.1002/QJ.3803, 2020.

Hersbach, H., Bell, B., Berrisford, P., Biavati, G., Horányi, A., Muñoz Sabater, J., Nicolas, J., Peubey, C., Radu, R., Rozum, I., Schepers, D., Simmons, A., Soci, C., Dee, D., and Thépaut, J-N.: ERA5 hourly data on single levels from 1940 to present, Copernicus Climate Change Service (C3S) Climate Data Store (CDS) [data set], https://doi.org/10.24381/cds.adbb2d47, 2023.

Hu, Q., Li, T., Deng, X., Wu, T., Zhai, P., Huang, D., Fan, X., Zhu, Y., Lin, Y., Xiao, X., Chen, X., Zhao, X., Wang, L., and Qin, Z.: Intercomparison of global terrestrial carbon fluxes estimated by MODIS and Earth system models, Sci. Total Environ., 810, 152231, https://doi.org/10.1016/J.SCITOTENV.2021.152231, 2022.

Huffman, G., Stocker, E., Bolvin, D., Nelkin, E., and Tan, J.: GPM IMERG final precipitation L3 1 d 0.1 degree × 0.1 degree v06, Greenbelt, MD, Goddard Earth Sciences Data and Information Services Center (GES DISC) [data set], https://doi.org/10.5067/GPM/IMERGDF/DAY/06, 2019.

Humphrey, V., Zscheischler, J., Ciais, P., Gudmundsson, L., Sitch, S., and Seneviratne, S. I.: Sensitivity of atmospheric CO_2 growth rate to observed changes in terrestrial water storage, Nature, 560, 628–631, https://doi.org/10.1038/s41586-018-0424-4, 2018.

Iturbide, M., Gutiérrez, J. M., Alves, L. M., Bedia, J., Cerezo-Mota, R., Cimadevilla, E., Cofiño, A. S., Di Luca, A., Faria, S. H., Gorodetskaya, I. V., Hauser, M., Herrera, S., Hennessy, K., Hewitt, H. T., Jones, R. G., Krakovska, S., Manzanas, R., Martínez-Castro, D., Narisma, G. T., Nurhati, I. S., Pinto, I., Seneviratne, S. I., van den Hurk, B., and Vera, C. S.: An update of IPCC climate reference regions for subcontinental analysis of climate model data: definition and aggregated datasets, Earth Syst. Sci. Data, 12, 2959–2970, https://doi.org/10.5194/essd-12-2959-2020, 2020.

Joiner, J., Guanter, L., Lindstrot, R., Voigt, M., Vasilkov, A. P., Middleton, E. M., Huemmrich, K. F., Yoshida, Y., and Frankenberg, C.: Global monitoring of terrestrial chlorophyll fluorescence from moderate-spectral-resolution near-infrared satellite measurements: methodology, simulations, and application to GOME-2, Atmos. Meas. Tech., 6, 2803–2823, https://doi.org/10.5194/amt-6-2803-2013, 2013.

Jung, M., Koirala, S., Weber, U., Ichii, K., Gans, F., Camps-Valls, G., Papale, D., Schwalm, C., Tramontana, G., and Reichstein, M.: The FLUXCOM ensemble of global land-atmosphere energy fluxes, Scientific Data, 6, 1–14, https://doi.org/10.1038/s41597-019-0076-8, 2019.

Jung, M., Schwalm, C., Migliavacca, M., Walther, S., Camps-Valls, G., Koirala, S., Anthoni, P., Besnard, S., Bodesheim, P., Carvalhais, N., Chevallier, F., Gans, F., Goll, D. S., Haverd, V., Köhler, P., Ichii, K., Jain, A. K., Liu, J., Lombardozzi, D., Nabel, J. E. M. S., Nelson, J. A., O'Sullivan, M., Pallandt, M., Papale, D., Peters, W., Pongratz, J., Rödenbeck, C., Sitch, S., Tramontana, G., Walker, A., Weber, U., and Reichstein, M.: Scaling carbon fluxes from eddy covariance sites to globe: synthesis and evaluation of the FLUXCOM approach, Biogeosciences, 17, 1343–1365, https://doi.org/10.5194/bg-17-1343-2020, 2020.

Kern, S.: MODIS Collection 6 global 8-daily Gross Primary Production (Version 2019_fv0.01), Uni Hamburg [data set], https://doi.org/10.25592/uhhfdm.8556, 2021.

Kim, D., Lee, M. I., Jeong, S. J., Im, J., Cha, D. H., and Lee, S.: Intercomparison of Terrestrial Carbon Fluxes and Carbon Use Efficiency Simulated by CMIP5 Earth System Models, Asia-Pac. J. Atmos. Sci., 54, 145–163, https://doi.org/10.1007/s13143-017-0066-8, 2018.

Knauer, J., Werner, C., and Zaehle, S.: Evaluating stomatal models and their atmospheric drought response in a land surface scheme: A multibiome analysis, J. Geophys. Res.-Biogeo., 120, 1894–1911, https://doi.org/10.1002/2015JG003114, 2015.

Kobayashi, S., Ota, Y., Harada, Y., Ebita, A., Moriya, M., Onoda, H., Onogi, K., Kamahori, H., Kobayashi, C., Endo, H., Miyaoka, K., and Kiyotoshi, T.: The JRA-55 Reanalysis: General Specifications and Basic Characteristics, J. Meteorol. Soc. Jpn. Ser. II, 93, 5–48, https://doi.org/10.2151/JMSJ.2015-001, 2015.

Köhler, P., Guanter, L., and Joiner, J.: A linear method for the retrieval of sun-induced chlorophyll fluorescence from GOME-2 and SCIAMACHY data, Atmos. Meas. Tech., 8, 2589–2608, https://doi.org/10.5194/amt-8-2589-2015, 2015.

Leuning, R.: A critical appraisal of a combined stomatal-photosynthesis model for C3 plants, Plant Cell Environ., 18, 339–355, https://doi.org/10.1111/j.1365-3040.1995.tb00370.x, 1995.

Liu, L., Ciais, P., Wu, M., Padrón, R. S., Friedlingstein, P., Schwaab, J., Gudmundsson, L., and Seneviratne, S. I.: Increasingly negative tropical water–interannual CO_2 growth rate coupling, Nature, 618, 755–760, https://doi.org/10.1038/s41586-023-06056-x, 2023.

Martens, B., Miralles, D. G., Lievens, H., van der Schalie, R., de Jeu, R. A. M., Fernández-Prieto, D., Beck, H. E., Dorigo, W. A., and Verhoest, N. E. C.: GLEAM v3: satellite-based land evaporation and root-zone soil moisture, Geosci. Model Dev., 10, 1903–1925, https://doi.org/10.5194/gmd-10-1903-2017, 2017.

Miralles, D. G., Holmes, T. R. H., De Jeu, R. A. M., Gash, J. H., Meesters, A. G. C. A., and Dolman, A. J.: Global land-surface evaporation estimated from satellite-based observations, Hydrol. Earth Syst. Sci., 15, 453–469, https://doi.org/10.5194/hess-15-453-2011, 2011.

Piao, S., Sitch, S., Ciais, P., Friedlingstein, P., Peylin, P., Wang, X., Ahlström, A., Anav, A., Canadell, J. G., Cong, N., Huntingford, C., Jung, M., Levis, S., Levy, P. E., Li, J., Lin, X., Lomas, M. R., Lu, M., Luo, Y., Ma, Y., Myneni, R. B., Poulter, B., Sun, Z., Wang, T., Viovy, N., Zaehle, S., and Zeng, N.: Evaluation of terrestrial carbon cycle models for their response to climate variability and to CO_2 trends, Global Change Biol., 19, 2117–2132, https://doi.org/10.1111/GCB.12187, 2013.

Pickering, M., Cescatti, A., and Duveiller, G.: Sun-induced fluorescence as a proxy for primary productivity across vegetation types and climates, Biogeosciences, 19, 4833–4864, https://doi.org/10.5194/bg-19-4833-2022, 2022.

Running, S., Mu, Q., and Zhao, M.: MOD17A2H MODIS/Terra Gross Primary Productivity 8-Day L4 Global 500 m SIN Grid V006 [data set], https://doi.org/10.5067/MODIS/MOD17A2H.006, 2015.

Running, S. W., Nemani, R. R., Heinsch, F. A., Zhao, M., Reeves, M., and Hashimoto, H.: A Continuous Satellite-Derived Measure of Global Terrestrial Primary Production, BioScience, 54, 547–560, https://doi.org/10.1641/0006-3568(2004)054[0547:ACSMOG]2.0.CO;2, 2004.

Schimel, D., Pavlick, R., Fisher, J. B., Asner, G. P., Saatchi, S., Townsend, P., Miller, C., Frankenberg, C., Hibbard, K., and Cox, P.: Observing terrestrial ecosystems and the carbon cycle from space, Global Change Biol., 21, 1762–1776, https://doi.org/10.1111/GCB.12822, 2015.

Seferian, R.: CNRM-CERFACS CNRM-ESM2-1 model output prepared for CMIP6 CMIP esm-hist, Version 20200715, Earth System Grid Federation [data set], https://doi.org/10.22033/ESGF/CMIP6.4003, 2019.

Seland, Ø., Bentsen, M., Oliviè, D. J. L., Toniazzo, T., Gjermundsen, A., Graff, L. S., Debernard, J. B., Gupta, A. K., He, Y., Kirkevåg, A., Schwinger, J., Tjiputra, J., Aas, K. S., Bethke, I., Fan, Y., Griesfeller, J., Grini, A., Guo, C., Ilicak, M., Karset, I. H. H., Landgren, O. A., Liakka, J., Moseid, K. O, Nummelin, A., Spensberger, C., Tang, H., Zhang, Z., Heinze, C., Iversen, T., and Schulz, M.: NCC NorESM2-LM model output prepared for CMIP6 CMIP esm-hist, Version 20200218, Earth System Grid Federation [data set], https://doi.org/10.22033/ESGF/CMIP6.7924, 2019.

Slevin, D., Tett, S. F. B., Exbrayat, J.-F., Bloom, A. A., and Williams, M.: Global evaluation of gross primary productivity in the JULES land surface model v3.4.1, Geosci. Model Dev., 10, 2651–2670, https://doi.org/10.5194/gmd-10-2651-2017, 2017.

Tang, Y., Rumbold, S., Ellis, R., Kelley, D., Mulcahy, J., Sellar, A., Walton, J., and Jones, C.: MOHC UKESM1.0-LL model output prepared for CMIP6 CMIP esm-hist, Version 20210122, Earth System Grid Federation [data set], https://doi.org/10.22033/ESGF/CMIP6.5929, 2019.

Tramontana, G., Jung, M., Schwalm, C. R., Ichii, K., Camps-Valls, G., Ráduly, B., Reichstein, M., Arain, M. A., Cescatti, A., Kiely, G., Merbold, L., Serrano-Ortiz, P., Sickert, S., Wolf, S., and Papale, D.: Predicting carbon dioxide and energy fluxes across global FLUXNET sites with regression algorithms, Biogeosciences, 13, 4291–4313, https://doi.org/10.5194/bg-13-4291-2016, 2016.

Ulaby, F., Moore, M., and Fung, A.: Microwave Remote Sensing, Active and Passive: Radar Remote Sensing and Surface Scattering and Emission Theory, vol. 2, Artech House, Norwood, MA, ISBN: 0890061939, 1982.

Wild, B., Teubner, I., Moesinger, L., Zotta, R.-M., Forkel, M., van der Schalie, R., Sitch, S., and Dorigo, W. A.: VODCA2GPP (Version 1.0.0), TU Wien [data set], https://doi.org/10.48436/1k7aj-bdz35, 2021.

Wild, B., Teubner, I., Moesinger, L., Zotta, R.-M., Forkel, M., van der Schalie, R., Sitch, S., and Dorigo, W.: VODCA2GPP – a new, global, long-term (1988–2020) gross primary production dataset from microwave remote sensing, Earth Syst. Sci. Data, 14, 1063–1085, https://doi.org/10.5194/essd-14-1063-2022, 2022.

Wong, B.: Color blindness, Nat. Methods, 8, 441, https://doi.org/10.1038/NMETH.1618, 2011.

Worden, J., Saatchi, S., Keller, M., Bloom, A. A., Liu, J., Parazoo, N., Fisher, J. B., Bowman, K., Reager, J. T., Fahy, K., Schimel, D., Fu, R., Worden, S., Yin, Y., Gentine, P., Konings, A. G., Quetin, G. R., Williams, M., Worden, H., Shi, M., and Barkhordarian, A.: Satellite Observations of the Tropical Terrestrial Carbon Balance and Interactions With the Water Cycle During the 21st Century, Rev. Geophys., 59, e2020RG000711, https://doi.org/10.1029/2020RG000711, 2021.

Wu, M., Vico, G., Manzoni, S., Cai, Z., Bassiouni, M., Tian, F., Zhang, J., Ye, K., and Messori, G.: Early Growing Season Anomalies in Vegetation Activity Determine the Large-Scale Climate-Vegetation Coupling in Europe, J. Geophys. Res.-Biogeo., 126, e2020JG006167, https://doi.org/10.1029/2020JG006167, 2021.

Wu, M., Manzoni, S., Vico, G., Bastos, A., de Vries, F. T., and Messori, G.: Drought Legacy in Sub-Seasonal Vegetation State and Sensitivity to Climate Over the Northern Hemisphere, Geophys. Res. Lett., 49, e2022GL098700, https://doi.org/10.1029/2022GL098700, 2022.

Wu, T., Chu, M., Dong, M., Fang, Y., Jie, W., Li, J., Li, W., Liu, Q., Shi, X., Xin, X., Yan, J., Zhang, F., Zhang, J., Zhang, L., and Zhang, Y.: BCC BCC-CSM2MR model output prepared for CMIP6 CMIP esm-hist, Version 20181220, Earth System Grid Federation [data set], https://doi.org/10.22033/ESGF/CMIP6.2901, 2018.

Zhang, Y., Xiao, X., Wu, X., Zhou, S., Zhang, G., Qin, Y., and Dong, J.: A global moderate resolution dataset of gross primary production of vegetation for 2000–2016, Scientific Data, 4, 1–13, https://doi.org/10.1038/sdata.2017.165, 2017a.

Zhang, Y., Xiao, X., Wu, X., Zhou, S., Zhang, G., Qin, Y., and Dong, J.: A global moderate resolution dataset of gross primary production of vegetation for 2000–2016, figshare [data set], https://doi.org/10.6084/m9.figshare.c.3789814.v1, 2017b.

Ziehn, T., Chamberlain, M., Lenton, A., Law, R., Bodman, R., Dix, M., Wang, Y., Dobrohotoff, P., Srbinovsky, J., Stevens, L., Vohralik, P., Mackallah, C., Sullivan, A., O'Farrell, S., and Druken, K.: CSIRO ACCESS-ESM1.5 model output prepared for CMIP6 CMIP esm-hist, Version 20191128, Earth System Grid Federation [data set], https://doi.org/10.22033/ESGF/CMIP6.4242, 2019.

Zobitz, J., Moore, D. J., Quaife, T., Braswell, B. H., Bergeson, A., Anthony, J. A., and Monson, R. K.: Joint data assimilation of satellite reflectance and net ecosystem exchange data constrains ecosystem carbon fluxes at a high-elevation subalpine forest, Agr. Forest Meteorol., 195, 73–88, https://doi.org/10.1016/j.agrformet.2014.04.011, 2014.